stellarator news

Published by Fusion Energy Division, Oak Ridge National Laboratory
Building 9201-2 P.O. Box 2009 Oak Ridge, TN 37831-8071, USA

Editor: James A. Rome Issue 81 May 2002
E-Mail: jar@ornl.gov Phone (865) 574-1306
On the Web at *http://www.ornl.gov/fed/stelnews*

An impurity accumulation density window in long-pulse LHD discharges

Impurity control is one of the important issues for realizing a fusion reactor. In particular, impurity behavior during steady-state operation is of special concern because neoclassical convection may cause strong inwardly directed drift velocities. Long-pulse discharges on the Large Helical Device (LHD) enable us to investigate impurity behavior with a long time scale in high-confinement stable plasmas without sawtooth crashes or edge-localized mode (ELM) activities. In a variety of long-pulse discharges [1–3], we found that metallic impurity accumulation was observed in hydrogen-only discharges in a narrow density window around 2×10^{19} m^{-3} [4]. Spectroscopic and bolometric measurements showed a remarkable temporal increase of core radiation due to metallic impurities in constant-density discharges. In this report, the impurity behavior in hydrogen long-pulse discharges heated by neutral beam injection (NBI) is described, and the density dependence is compared with neoclassical predictions.

Impurity accumulation in constant-density discharges

In LHD, long-pulse discharges have been mainly carried out with helium gas, including a small amount of hydrogen for ion cyclotron radio frequency (ICRF) H-minority heating or hydrogen beam particles from NBI heating. In these discharges, there was no fatal impurity accumulation and the impurity level was maintained constant until the end of the discharge [3]. However, impurity accumulation behavior was first observed when extending the discharge duration in long-pulse operation with hydrogen gas puffing. Figure 1 shows a typical constant-density discharge with impurity accumulation. The NBI heating power is about 1.7 MW, and the plasma density is kept constant at 2.7×10^{19} m^{-3}. In this case, the radiated power density S_{rad} at $\rho = 0.945$ and the impurity line emissions (Fe XVI, C III) originating from the peripheral region of the plasma remain almost constant during the discharge, while at $\rho = 0$, S_{rad} increases and the central electron temperature decreases, thereby leading to a reduction of the stored energy. A remarkable change of impurity behavior was seen in a density scan. Figure 2 shows the time evolution of the central radiated power density and the most prominent metallic emission (Fe XXIII), which originates from the central region of the plasma, for discharges with different plasma densities. Remarkable temporal increases of the central radiation and the iron line emission occurred only for the discharge with $\bar{n}_e = 2.7 \times 10^{19}$ m^{-3}. For other discharges, all observable quantities remained almost constant during the discharge ($\tau_d = 10$ s).

In this issue . . .

Impurity density profiles

Assuming that the radiation in the core region is due to iron impurities only, we calculated the impurity concentration and the radial profile by coupling a one-dimensional (1-D) impurity transport code (MIST) with measured plasma density and temperature profiles. Figure 3 shows the analyzed discharge waveform and the central iron density estimated by the MIST code for a density ramp-up discharge. The central radiated power density increases remarkably with density and then decreases in the high-density region, even though there is no significant change in S_{rad} at the peripheral region. The central iron density in Fig. 3(d) was estimated by the radiation emissivity at the plasma center from bolometry measurements, assuming a radially constant diffusion coefficient of 0.1 m^2/s, as observed in several helical devices [5]. The central iron density $n_{Fe}(0)$ increases after the average electron density exceeds about 1×10^{19} m^{-3} and reaches a maximum of 4.5×10^{16} m^{-3} at around $\bar{n}_e = 2.7 \times 10^{19}$ m^{-3}. Thereafter, $n_{Fe}(0)$ decreases with increasing electron density.

On the other hand, no significant change in the brightness of the Fe XVI spectral line, originating from the peripheral plasma, was observed during the increase in $n_{Fe}(0)$. The impurity emission increases because of the reduction of the electron temperature, in spite of the decrease of iron density in the central region.

The iron density profiles were estimated by fitting the calculated and measured radiated power density profiles as shown in Fig. 4. In this calculation, the diffusion coefficient was constant (D = 0.1 m^2/s) and the convection velocity dependence on radius was adjusted so that the radiation profile from bolometry measurements was reproduced in the core region [$V(r)$ = 0–2 m/s]. In this figure, one can see clear evidence of impurities accumulating and diffusing out. In the initial stage of the discharge (t = 2 s), the radiation profile is hollow, as seen in short-pulse discharges [6], and the iron density profile is nearly flat. However, the radiation profile becomes peaked with time or with increasing density, and strong core radiation is observed at t = 7.3 s [Fig. 4(a)]. On the other hand, a strong peaking of the iron density is observed at t = 5.5 s, and the profile becomes flat at t = 7.3 s [Fig. 4(b)]. Thus, the MIST code analysis shows that metallic impurities accumulate in the density range of $\bar{n}_e \sim (1 - 2.7) \times 10^{19}$ m^{-3} and diffuse out of the plasma core at higher density.

Density window of impurity accumulation

As described above, the impurity behavior in long-pulse discharges largely depends on the operational plasma density. Figure 5 shows the dependence of the central iron density on the line-averaged electron density in both density ramp-up discharges and constant-density discharges with P_{NBI} = 1.5 MW. From this figure, we can find a density window of impurity accumulation for NBI-heated pure hydrogen discharges. In the low-density region ($\bar{n}_e \leq 1 \times 10^{19}$ m^{-3}), there is no sign of impurity accumulation even for long-pulse discharges lasting more than 10 s. When the plasma density exceeds 1.5×10^{19} m^{-3}, a significant increase in central radiation due to metallic impurities is observed, and impurity contamination becomes severe with increasing density. However, as the plasma passes through the density window of

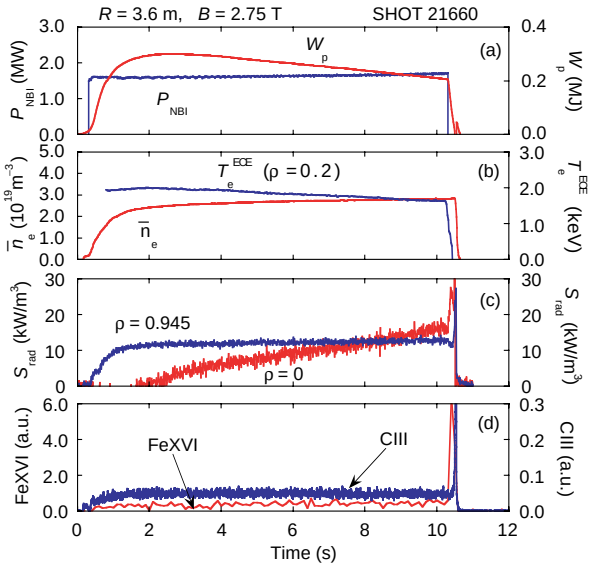

Fig. 1. A typical constant-density discharge with impurity accumulation. The plasma density is kept constant by a gas puffing system with a feedback loop.

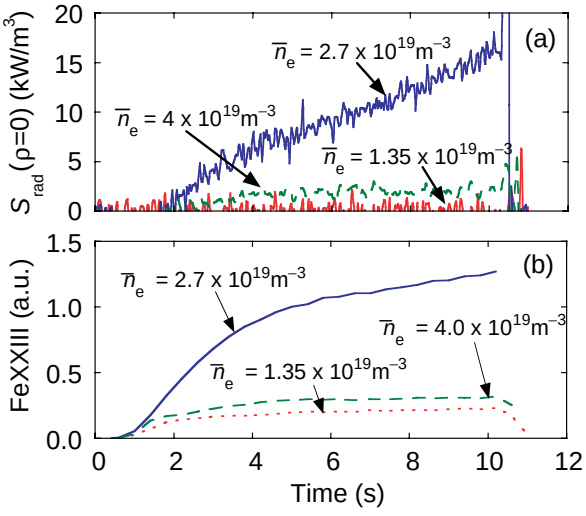

Fig. 2. Time evolution of (a) central radiation and (b) Fe XXIII emission for the discharges with constant densities. Remarkable increases are observed only for the discharge with the density of 2.7×10^{19} m^{-3}.

$\bar{n}_e \sim (1-2.7)\times 10^{19}$ m^{-3}, the accumulated impurities diffuse out and the impurity density decreases remarkably. In the high-density region ($\bar{n}_e > 4\times 10^{19}$ m^{-3}), there is again no sign of impurity accumulation, as in the low-density region. The density range of impurity accumulation shifted slightly to a higher-density region with increasing NBI power.

Impurity transport regimes

In order to understand the density dependence of impurity accumulation, we tried to distinguish the impurity behavior in a *n*-*T* diagram, taking into account the various impurity transport regimes of neoclassical impurity transport theory [7, 8]. In Fig. 6, plasmas in a variety of long-pulse discharges are plotted according to their density and temperature at the plasma center, and classified by the impurity behavior. The solid line represents the transition between the plateau regime and the Pfirsch-Schlüter (PS) regime for iron impurity. The dashed line represents the transition between the electron root and the ion root for the background plasma. Neoclassical analysis shows that the radial impurity flux is dominated by the convection component, which changes sign (inward or outward) for different impurity transport regimes. On the whole, the observed impurity behavior is in qualitative agreement with neoclassical impurity transport. In the low-density and high-temperature region, high-*Z* impurities may be expelled by the positive radial electric field or diffuse out because of nearly zero electric field. As indicated in Fig. 6, it is not so easy to obtain the electron root in the plasma core, but it is possible to obtain it in the peripheral region [9]. Furthermore, small positive electric fields were observed even in the density range of the ion root near the transition to the electron root [9, 10]. The boundary of impurity accumulation in the low-collisionality regime may be shifted to a higher collisionality regime. In the intermediate regime with negative radial electric field (ion root), the high-*Z* impurities are accumulated in the central plasma because of the electric field in the $1/\nu$ regime or the temperature gradient in the plateau regime. When impurities enter in the PS regime, they are screened by the dominant contribution of the temperature gradient term on account of the flat density profile and the parabolic temperature profile, which are usually observed in LHD plasmas.

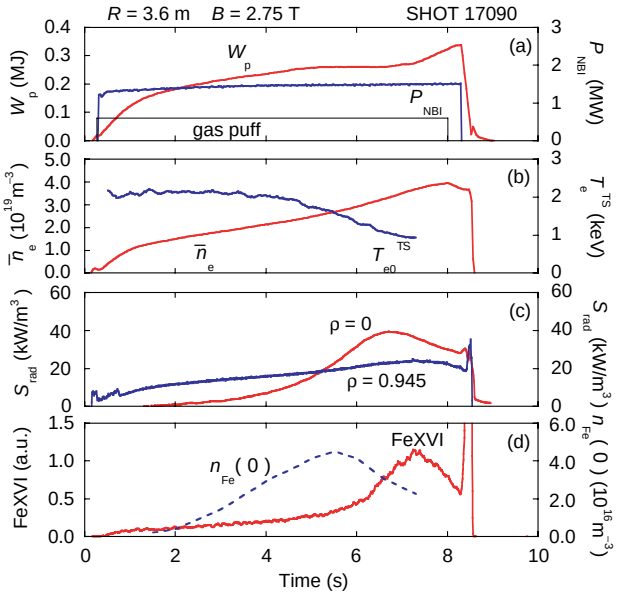

Fig. 3. Time evolution of plasma parameters and the central iron density in a density ramp-up discharge (shot 17090). The plasma density increases with time as a result of constant gas puffing. The central iron density $n_{Fe}(0)$ was estimated by the impurity transport code MIST.

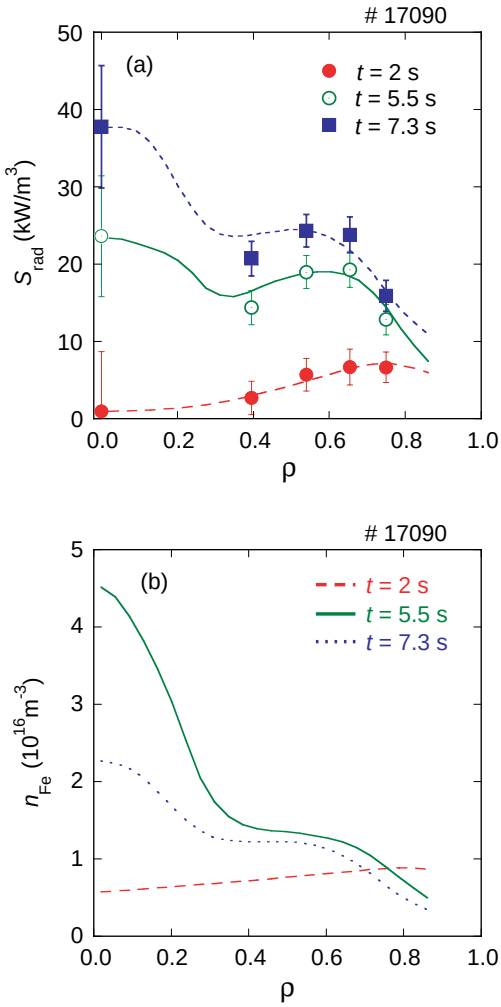

Fig. 4. Radial profiles of (a) radiated power density from bolometry measurements and (b) iron density from MIST code simulations at various times for shot 17090. The metallic impurities accumulate\d until 5.5 s and then diffuse\d out, leading to a flat profile.

Y. Nakamura and the LHD experimental group
National Institute for Fusion Science
322-6 Oroshi-cho, Toki 509-5292, Japan
E-mail: ynakamu@lhd.nifs.ac.jp

References

[1] Y. Takeiri, Y. Nakamura, et al., Plasma Phys. Controlled Fusion **42** (2000) 147.

[2] Y. Nakamura et al., J. Nucl. Mater. **290**–**293** (2001) 1040.

[3] N. Noda, Y. Nakamura, et al., Nucl. Fusion **41** (2001) 779.

[4] Y. Nakamura et al., submitted to Plasma Phys. Controlled Fusion (2002).

[5] H. Kaneko et al., Nucl. Fusion **27** (1987) 1075.

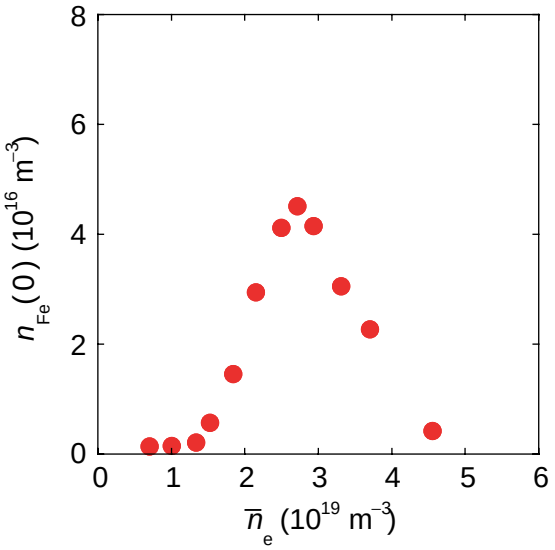

Fig. 5. Density window of impurity accumulation for NBI-heated hydrogen plasmas with P_{NBI} = 1.5 MW. The central iron density is plotted as a function of the density for both density ramp-up discharges and constant-density discharges.

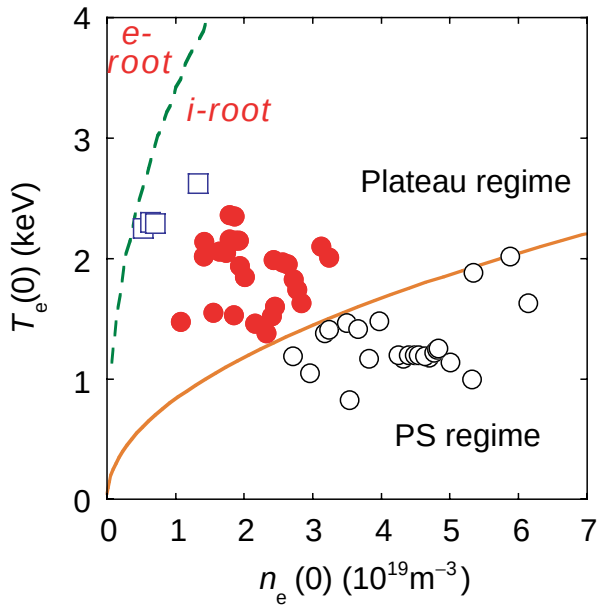

Fig. 6. Impurity behavior in long-pulse discharges. The solid circles indicate plasmas with impurity accumulation. The open squares indicate plasmas without accumulation. The open circles indicate plasmas with a decrease of impurities or without impurity accumulation.

Diagnostic development and plasma reconstruction for low-aspect-ratio stellarators

A group of theoreticians and experimentalists with backgrounds in stellarator and tokamak physics has assembled to begin development of a new stellarator reconstruction and data analysis code. This code will provide capabilities for stellarator diagnostic analysis ([ncluding magnetics and motional Stark effect (MSE) diagnostics] that will be comparable to those presently provided for tokamaks by the world-renowned EFIT [1] code. Because of its three-dimensional (3-D) character, the code will also provide a capability for analysis of departures from axisymmetry in tokamak plasmas.

The capability for equilibrium reconstruction from experimental data is used routinely for tokamak plasmas with presumed axisymmetry. However, only a limited capability exists to perform such analysis for non-axisymmetric configurations [2,3]. As β rises in stellarators, and for compact (low-aspect-ratio), hybrid configurations with net plasma current, such as envisioned for the National Compact Stellarator Experiment (NCSX), Quasi Poloidal Stellarator (QPS), and the Compact Toroidal Hybrid (CTH) experiments, this capability will become increasingly important for accurate equilibrium analysis. Previous study of discharge evolution in the proposed NCSX device has shown that active control of the helical field, in addition to the poloidal field, is required to maintain attractive quasi-symmetry and stability properties as the plasma pressure and current depart from the vacuum state. This will require magnetic diagnostics with the capability to detect non-axisymmetric changes in the plasma boundary shape. The code now under development will be structured to interface readily to stellarator data acquisition systems and is envisioned to become a cornerstone of experimental analysis in a way analogous to the worldwide use of EFIT on tokamaks.

As a first step, we have begun to generalize the magnetic diagnostic analysis capabilities of EFIT into three dimensions. In general, we wish to compute the flux ψ_i through a diagnostic flux loop (labeled *i*) in response to external coil currents I_j^c (labeled *j*) and internal plasma currents (J_p). Using Stokes' theorem, we can write:

$$\Psi_i \equiv \iint \mathbf{B}\cdot d\mathbf{S}_i = \oint \mathbf{A}\cdot d\mathbf{l}_i$$
$$\mathbf{A} = \sum_{j=\text{ext.coils}} \mathbf{a}_j^c I_j^c + \mathbf{A}_p \qquad (1)$$

Here, $\mathbf{A}$ is the vector potential, $\mathbf{a}_j^c$ is the vector potential due to unit current in the *j*th external coil, and $\mathbf{A}_p$ is the vector potential due to the plasma current. The contribution to the flux from the external coils can be written in terms of the mutual inductance matrix:

$$\Psi_i^{\text{ext}} = \sum_j L_{ij} I_j^c$$
$$L_{ij} = \oint \mathbf{a}_j^c \cdot d\mathbf{l}_i \qquad (2a)$$

This is a generalization to three dimensions of the inductance matrix previously computed for an axisymmetric plasma [4]. It follows from the symmetry with respect to interchange of the observation and source points of the geometric part of the Biot-Savart kernel, $|\boldsymbol{r}-\boldsymbol{r}'|$, that L_{ij} is a symmetric matrix. Thus, the flux enclosed by the *j*th external coil, due to a virtual unit current in the *i*th diagnostic loop, is the same as the flux in the *i*th diagnostic loop due to a unit current in the *j*th external coil. We can use this reciprocity to compute L_{ij} in the following equivalent form:

$$L_{ij} = \oint \mathbf{a}_i^d \cdot d\mathbf{l}_j^c \qquad (2b)$$

Here, $\mathbf{a}_i^d$ is the vector potential due to unit current in the *i*th diagnostic coil. The integration path in Eq. (2b) is over the *j*th closed external coil. The physical interpretation of Eq. (2b) is that the flux through each diagnostic loop can be uniquely, and completely, characterized by its vector potential $\mathbf{a}_i^d$.

To efficiently evaluate L_{ij}, we have developed a fast numerical routine for computing $\mathbf{a}_j^d$ for arbitrary diagnostic loops approximated by multiple connected straight-line segments. The calculation is based on a simple analytic expression for the vector potential of a unit current straight-line current filament:

$$\mathbf{a}_{\text{seg}}(\mathbf{x}) = \frac{\mu_0}{4\pi}\mathbf{e}\ln\left(\frac{R_f + R_i + L_{\text{seg}}}{R_f + R_i - L_{\text{seg}}}\right) \qquad (3)$$

Here, $\mathbf{e}$ is the unit vector in the direction of the coil segment, L_{seg} is the length of the coil segment, and $R_{i,f}$ is the distance between the observation point $\mathbf{x}$ (where $\mathbf{a}_{\text{seg}}$ is computed) and the initial (*i*) [or final (*f*)] point on the coil segment.

The routine is capable of computing vector potential contributions to the line integral in Eq. (2) at a rate of up to 7×10^6 segments per second on a Pentium 4-class PC. The use of a Taylor or Padé approximation for the evaluation of the natural logarithm is being tested and initial indi-

cations are that the code performance is improved to nearly 20×10^6 segments per second.

Using the Biot-Savart law to express $\mathbf{A}_p$ in terms of the internal plasma currents, a formula has been derived from which the plasma flux response (for a given equilibrium current) can be readily obtained:

$$\Psi_i^p = \iiint \mathbf{J}_p(\mathbf{x}') \cdot \mathbf{a}_i^d(\mathbf{x}') d^3\mathbf{x}' \tag{4}$$

Here, $\mathbf{a}_j^d$ is the *same* vector potential appearing in Eq. (2b). It is given explicitly as follows:

$$\mathbf{a}_i^d(\mathbf{x}) = \frac{\mu_0}{4\pi} \oint d\mathbf{l}_i \mid \mathbf{x} - \mathbf{r}(\mathbf{l}_i) \mid^{-1} \tag{5}$$

In Eq. (5), $\mathbf{r}(\mathbf{l}_i)$ represents the boundary curve of the *i*th flux loop. Since the plasma current in Eq. (4) is anticipated to be computed from a flux-coordinate based equilibrium code, such as VMEC [5], we evaluate the volume integral in Eq.(4) in flux coordinates as follows:

$$\Psi_i^p = \int_p d\varphi_p d\theta ds \sqrt{g} \left[J^\theta \left(R_\theta a'_{iR} + Z_\theta a'_{iZ} \right) + J^\varphi \left(R_\varphi a'_{iR} + R a'_{i\varphi} + Z_\varphi a'_{iZ} \right) \right] \tag{6}$$

Here, the primes on the cylindrical components of the vector potential denote sums over the self-similar field periods of the stellarator. This reduces the toroidal angle integration in Eq. (6) to a single field period. Since these cylindrical components of $\mathbf{a}_j^d$ are *independent* of the plasma equilibrium, they may be precomputed and stored on a uniform R,φ,Z mesh (limited to a single field period, reducing the storage requirements when $N_p > 1$) for subsequent use (via interpolation) in the rapid calculation of the flux responses for various plasma equilibria. Observe that the coefficients of the current density components in Eq. (6) can be interpreted physically as distributed inductance coefficients by comparing with Eq. (2a).

The flux response in Eq. (6) has been written in anticipation of future reconstruction capabilities of this code, for which regression analysis will be used to determine the flux-signal dependence on the internal plasma profiles (pressure and rotational transform). If *only* the external flux response is required, then Eq. (4) can be converted (using the virtual casing principle [6]) into a surface integral (which is more efficient to evaluate numerically) over the plasma-vacuum interface:

$$\Psi_i^p = \frac{1}{\mu_0} \iint \mathbf{B}(\mathbf{x}') \times \mathbf{a}_i^d(\mathbf{x}') \cdot d\mathbf{S} \tag{7}$$

An alternative, but equivalent, expression for the flux response can be obtained from Eq. (4) of Ref. 2.

Previous comparison of external magnetic fields using relations similar to Eqs. (4) and (7) have been made at large aspect ratio ($A \sim 7$). We plan to extend this comparison to the lower aspect ratios characterizing the new stellarator devices presently under construction or development in the United States. In particular, this comparison will be useful in assessing the accuracy with which numerical 3D-equilibria need to be computed at low aspect-ratios to provide accurate external flux responses.

A first application of this new code will be the design of magnetic diagnostics for NCSX, QPS, and CTH. For NCSX, these will be capable of providing the real-time plasma shape control needed for stable evolution of the discharge to high β.

References

[1] L. L. Lao et.al., Nucl. Fusion **25** (1985) 1611.

[2] H. Gardner, Nucl. Fusion **30** (1990) 1417..

[3] R. N. Morris, et. al, Nucl. Fusion **29** (1989) 2115; E. Strumberger, Nucl. Fusion **37** (1997) 19.

[4] S. P. Hirshman and G. H. Neilson, Phys. Fluids **29** (1986) 790.

[5] S. P. Hirshman and J. C. Whitson, Phys. Fluids **26** (1983) 3553.

[6] V. D. Shafranov and L. E. Zakharov, Nucl. Fusion **12** (1972) 599.

Submitted by S. P. Hirshman
On behalf of L. Lao, E. Lazarus, J. Hanson, and S. Knowlton
E-mail: HirshmanSP@ornl.gov